DISCLAIMER

ORNL/TM-2025/4149

Report on the Integration of Experimental and Modeling Data for Initial Equivalence Study of LPBF 316 Stainless Steel

Stephen Taller
Geeta Kumari

Approved for public release.
Distribution is unlimited.

September 2025

M3MT-25OR0904031

OAK RIDGE National Laboratory

ORNL IS MANAGED BY UT-BATTELLE LLC FOR THE US DEPARTMENT OF ENERGY

ORNL/TM-2025/4149

Advanced Materials and Manufacturing Technologies Program

REPORT ON THE INTEGRATION OF EXPERIMENTAL AND MODELING DATA FOR INITIAL EQUIVALENCE STUDY OF MECHANICAL PERFORMANCE IN IRRADIATED LPBF 316 SS

Stephen Taller, Geeta Kumari

Oak Ridge National Laboratory

September 2025

M3MT-25OR0904031

Acknowledgements:
Jim Horenburg, Sarah Graham, Kevin Hanson, Erik Herbert, Caleb Massey, Stephen Raiman, Mohammad Umar Farooq Khan, David Collins, Jesse Werden, Anthony Guajardo, Jerid Metcalf, Clay Morris, Nick Russell

Prepared by
OAK RIDGE NATIONAL LABORATORY
Oak Ridge, TN 37831
managed by
UT-BATTELLE LLC
for the
US DEPARTMENT OF ENERGY
under contract DE-AC05-00OR22725

This page intentionally left blank.

CONTENTS

LIST OF FIGURES

LIST OF TABLES

ABBREVIATIONS

AMMT	Advanced Materials and Manufacturing Technologies
ASME	American Society of Mechanical Engineers
BD	build direction
HFIR	High Flux Isotope Reactor
LAIN	Licensing Approach with Ions and Neutrons
LPBF	laser powder bed fusion
MIBL	Michigan Ion Beam Laboratory
SA	solution-annealed
SR	stress-relieved
TD	transverse direction
YS	yield strength

ABSTRACT

To ensure the rapid development, deployment, and use of advanced nuclear technologies, faster qualification approaches are needed. Typically, the primary pathway uses traditional data packages consistent with the American Society of Mechanical Engineers Boiler and Pressure Vessel Code, which does not consider the environmental effects the material will experience such as corrosion and radiation damage. Examining radiation effects requires a significant amount of space in US facilities at the Advanced Test Reactor and the High Flux Isotope Reactor (HFIR) and suffers from natural gradients in temperature and neutron flux profiles. Ion irradiation may enable rapid assessment of radiation-induced damage to a material and is proposed as part of an accelerated materials qualification framework through the Advanced Materials and Manufacturing Technologies program. To enhance the utility of ion irradiation as an examination tool, this report provides the initial assessment of engineering-relevant properties of microstructures produced from ion irradiation in the near-surface volume. Nanoindentation, Vickers hardness, and known tensile properties were brought together with simple mathematical models and experimental data for an initial equivalence study of the mechanical performance of irradiated laser powder bed fusion (LPBF) 316 stainless steels across length scales. Direct observation of the calculated ion irradiation yield stress and measured neutron irradiation yield stress at 2 dpa showed that both datasets exhibit the same trend with irradiation temperature and overlap within an acceptable band of stress values. Ion irradiations at 10 dpa serve as a prediction of properties to compare to postirradiation examination of HFIR-irradiated LPBF 316H further in the program. This work is a significant demonstration of the Licensing Approach with Ions and Neutrons, which uses ion irradiations to generate mechanical property information more rapidly than through neutron irradiations.

1. INTRODUCTION

The motivation for the Advanced Materials and Manufacturing Technologies (AMMT) program is to accelerate the development, qualification, and manufacturing technologies to enable reliable and economical nuclear energy. Typically, the primary pathway uses traditional data packages consistent with the American Society of Mechanical Engineers (ASME) Boiler and Pressure Vessel Code [1]. However, pursuing qualifications along this pathway does not consider the environmental effects the material will experience. Therefore, additional testing is needed to generate environmental data, such as corrosion or radiation effects data, relevant to nuclear environments. ASME-style data packages typically require physically “large” specimens [2], which require a significant amount of space in US materials test facilities at the Advanced Test Reactor and the High Flux Isotope Reactor (HFIR) and suffer from natural gradients in temperature and neutron flux profiles. A recent examination of the state of the art for neutron irradiation experiments provided recommendations for standardizing irradiation experiments to accelerate nuclear materials qualification [3] and suggests that subsize specimens may provide a solution to minimize inherent gradients. The ability to obtain representative properties from small volumes is still an active area of research [4] and, for neutron irradiations, remains limited by the time required to achieve an adequate level of exposure or displacement damage (dpa). To ensure the rapid development, deployment, and use of advanced nuclear technologies (90 FR 22581 [5]), faster approaches are needed. Ion irradiation may enable rapid assessment of radiation-induced damage to a material and is proposed as part of an accelerated materials qualification framework as part of the AMMT program [6, 7]. Therefore, obtaining engineering-relevant properties using microstructures produced from ion irradiation in the near surface volume would greatly enhance the utility of ion irradiation as an examination tool.

As proposed in a previous AMMT report [8] in FY 2025 and FY 2026, the primary foci would be (1) continuing the microstructure-modeling approach and (2) determining how to extract performance-relevant data from the ion-irradiated microstructures and benchmark the process with neutron-irradiated specimens. Whether through low-temperature failure modes as estimated through the strength required to

fracture [9], high-temperature failure modes as the boundary for creep, or as a design limit for engineering applications, the yield strength (YS) is a defining performance property. Thus, YS is targeted as the figure of metric or property of interest in Step 1 of the Licensing Approach with Ions and Neutrons (LAIN) [6]. YS can be obtained from the microstructure of the material via several possible pathways, and these are outlined in Figure 1.

The most direct path from the microstructure to YS is through the dispersed barrier model built on the Taylor relation, where modifications to the YS depend on the size and density of microstructural obstacles to dislocation motion (e.g., dislocation loops, precipitates, grain boundaries, and solutes) and strength through the Orowan mechanism. Although the figure shows this equation as being linear additions, more generally the obstacles are divided by how weak or strong the obstacle is to dislocation motion, and a superposition method is applied [10, 11]. The strength of each obstacle is quantified by a factor, α, which can be thought of as the propensity of the dislocation to climb over or shear through the obstacle and depends on the size and shape of the obstacle and the temperature. Although this approach has been somewhat successful, in many cases the strength factors are determined via numerical fits to limited experimental data. Therefore, this report presents some work on how to approach this direct pathway, but detailed efforts are left for future work.

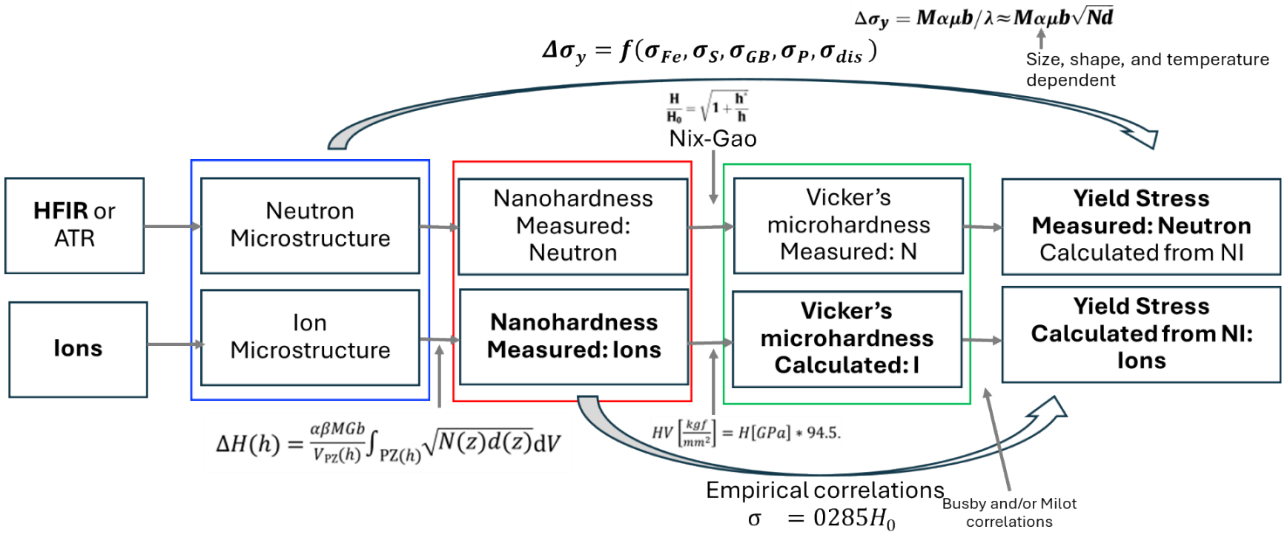

Figure 1. Approach to link microstructure with nanohardness, microhardness, and yield stress [8]. Items in bold are discussed throughout this report.

The second path, which is the focus of this report, is to measure another mechanical property and link this property to YS. The shallow penetration of ion irradiation severely limits the amount of mechanical information that can be collected in such a volume, making nanoindentation the primary technique for mechanical assessment. Recent work using the continuous stiffness method demonstrated nearly identical responses for neutron- and ion-irradiated ferritic–martensitic steels [10, 12, 13]. Therefore, in this path to measure the mechanical performance of a thin ion-bombarded surface, nanohardness would be measured from both neutron and ion irradiations and compared with the microstructure to determine the factors necessary to predict hardness.

The objective of this study was to combine simple mathematical models and experimental data for an initial equivalence study of the mechanical performance of irradiated laser powder bed fusion (LPBF) 316 stainless steels using nanoindentation, Vickers hardness, and known tensile properties to develop correlations across length scales. The overall goal for Oak Ridge National Laboratory in FY 2025 was to

exercise the irradiation challenge program [14] by generating initial predictions of neutron-irradiated hardness or YS at 10 dpa for one LPBF AM316 steel sample irradiated at 600°C. A proposed approach to link the microstructure and tensile properties directly is included as a guide for future work. The correlations presented in the remainder of this report progress from larger length scales to smaller length scales (i.e., from right to left in Figure 1).

2. METHODS TO DEVELOP CORRELATIONS

Although each aspect of the work performed has detailed information to develop the correlations, the methodologies of each study share some commonalities. This section presents several techniques and analysis methods that are used throughout the report.

2.1 TENSILE TESTING

SSJ2 specimens were tested in a shoulder-loading configuration under ambient conditions using a single-column Instron servomechanical test frame. A nominal strain rate of 0.015 (mm/mm)/min was applied for room-temperature measurements. During testing, time, crosshead displacement, load, and gauge cross-section dimensions were recorded. Because strain was not measured directly but derived from crosshead displacement, a compliance correction method was applied to extract approximate plastic strain values from the displacement data. The plastic strain, ε_p, was calculated as shown in Eq. (1):

$$\varepsilon_{\mathrm{p}} = \frac{\delta - P \times C_{\mathrm{LL}}}{l}, \#(1)$$

where δ is the crosshead displacement, P is the load, C_{LL} is the load-line compliance (calculated as the inverse of the elastic slope of the raw load–displacement curve), and l is the gauge length. Conversion of the load–displacement curve into a stress–plastic strain curve allowed calculation of the tensile properties. The 0.2% offset YS was defined as the stress at 0.2% plastic strain, the ultimate tensile strength as the maximum stress, the uniform elongation as the plastic strain corresponding to the ultimate tensile strength, and the total elongation as the plastic strain at failure.

2.2 INDENTATION EXPERIMENTS

Vickers hardness was measured using a pyramidal diamond indenter on a Carat 930 hardness tester with a load of 200 gf and dwell time of 10 s. Optical imaging of the dimensions of the resulting indentation creator measured the length and width of the crater to convert to Vickers hardness using Eq. (2), where F is the applied force, A is the area of the indent, and d is the length of a diagonal line across the rectangle containing the indent area. At least 25 points were sampled from each specimen to generate adequate statistics for analysis.

$$HV = \frac{F}{A} \sim \frac{1.8544F}{d^2} \left[\frac{kgf}{mm^2}\right], \#(2)$$

Instrumented indentation testing, colloquially nanoindentation, experiments were performed on a KLA iMicro Nanoindenter dedicated to nuclear fuels and materials at Oak Ridge National Laboratory. Indents were performed in either a 5 × 5 or a 6 × 6 array (total of either 25 or 36 points) for each specimen at room temperature using a Berkovich tip and a 50 mN actuator. The indenter performed advanced nanoindentation techniques using the continuous stiffness method [15, 16]. This technique provides a small oscillation to the indenter tip and allows for the determination of hardness and the elastic modulus through the entire depth of the indentation test. Instead of a fixed frequency and amplitude as commonly used in literature for irradiated materials [12, 13], this work used a fixed frequency of 110 Hz with a

variable amplitude equal to 10% of the applied load. Thus, as the indenter uses a higher applied load to push to deeper depths, the corresponding increase in amplitude keeps the signal-to-noise ratio at a minimal level. The indentation system was calibrated using fused silica, and the reference fused silica was checked before and after each series of indentations. The data from each individual indent are collated to form average curves for hardness vs. displacement and elastic modulus vs. displacement. To facilitate analysis, each average hardness curve was analyzed with the framework of the Nix–Gao law for strain gradient plasticity to account for size effects [17]. Equation (3) is the result of the original Nix–Gao derivation, and Eq. (4) is the same equation rewritten to a linear form. In these equations, H is the measured hardness, h is the displacement by the indenter, h^* is the characteristic length at which size effects are negligible, and H_0 is the bulk equivalent hardness. Although H_0^2 is multiplied by 1 and $1/h$, as the term $1/h$ approaches zero (h approaches infinity), this term becomes negligible. Thus, plotting the hardness squared as a function of the inverse displacement allows for the extrapolation of the linear fit of the data to "infinite" depth, becoming the bulk equivalent hardness, H_0.

$$\frac{H}{H_0} = \sqrt{1 + \frac{h^*}{h}} \#(3)$$

$$H^2 = H_0^2\left(1 + \frac{h^*}{h}\right) \#(4)$$

3. CORRELATIONS ACROSS LENGTH SCALES

The first step to develop or confirm correlations across length scales is to identify a set of samples containing many of the same microstructural features as irradiated materials to serve as an example set. Specimens from a study for post-build stress-relief optimization in the AMMT program [18] provided LPBF 316H in the as-printed condition with dislocation cell structures and with various combinations of annealing temperatures within a temperature range of 650°C–850°C with heating rate of 10°C/min using a box furnace and times ranging from 15 min to 6 h followed by air cooling to reduce the density of dislocations and form precipitates. The heat-treated samples were metallographically prepared for microstructural evaluation to a final finish of 0.05 μm with colloidal silica. Representative micrographs [18] are reproduced here to show the evolution of the dislocation cell density with time and temperature. The dissolution of dislocation cells is reminiscent of the evolution under irradiation [19] and thus can serve as a surrogate model for this aspect of the irradiated microstructures.

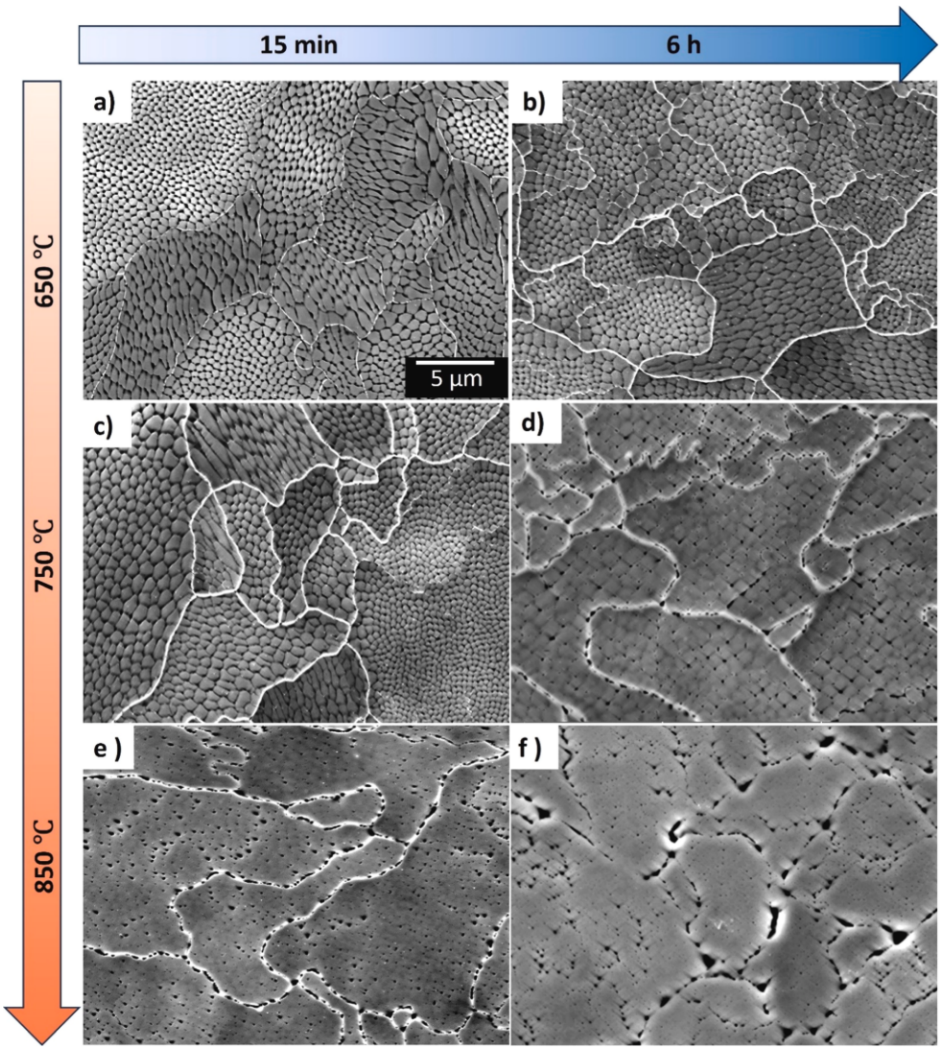

Figure 2. Secondary electron scanning electron micrographs of the etched samples heat-treated at 650°C, 750°C, or 850°C for either 15 min or 6 h [18]. All the micrographs are at the same magnification and have the same scale as the top left figure.

3.1 REVISITING THE RELATIONSHIP BETWEEN YIELD STRESS AND VICKERS HARDNESS

Based on the methods presented in Sections 2.1 and 2.2, both Vickers hardness and YS were collected to obtain a correlation between them. For this study, the aged specimens underwent testing along the build direction (BD) and in the transverse direction (TD). Vickers hardness was measured on the nonstressed regions of the tensile head to avoid the work-hardened areas and provide a direct comparison to select as-aged microstructures. A diagram of the orientation of the indents relative to a reference block is in Figure 3. Standard linear regression methods considering both BD and TD as one dataset yielded the curves shown in Figure 4 along BD and TD. The BD and TD datasets are noticeably different. The relationship between yield stress and Vickers hardness for the BD is about 1.5× that of the TD. The *y*-intercepts also suggest the microstructure in the BD samples is inherently stronger than that in the TD. When both are considered as one dataset, the slope and intercept meet in the middle of the two directions, suggesting that correlation is without the preferential texturing typically observed in the BD [20].

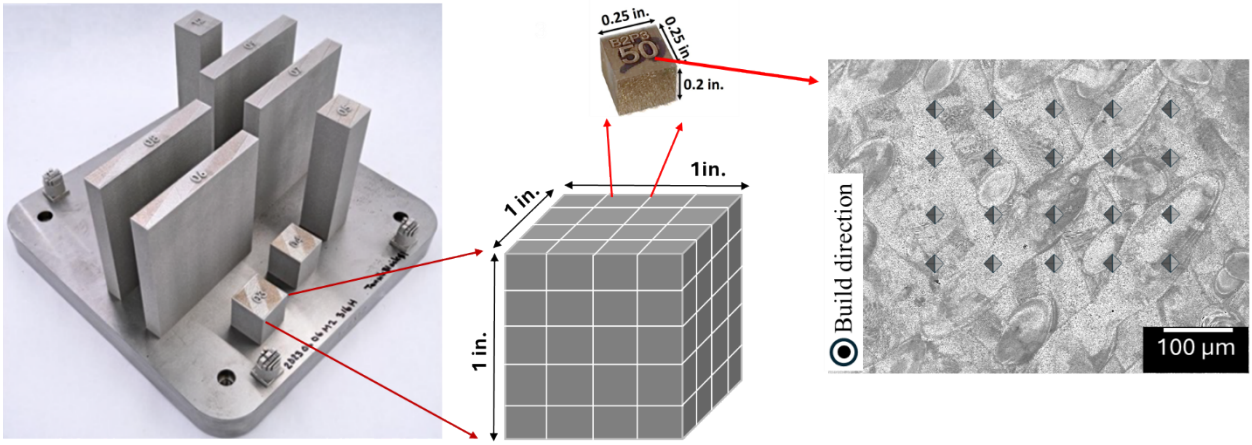

Figure 3. Schematic illustrating the orientation of the indentations relative to the LPBF build plate.

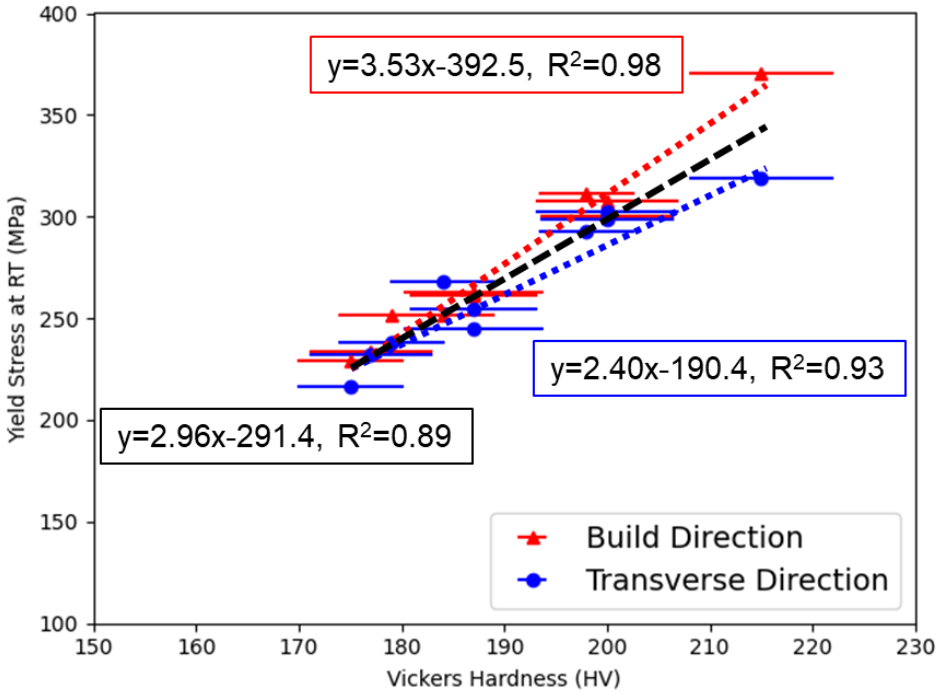

Figure 4. Comparison of Vickers hardness and YS for aged LPBF 316H specimens. Shown are the linear correlations along the BD (red), TD (blue), and the combination of both datasets (black).

The slope of the combined dataset is about 3, which is not surprising. Several previous correlations between Vickers hardness and YS resulted in slopes near 2.82 [21], 2.96 [22], and 3.06 [23] for nontextured steels and metals. Thus, this additional dataset from LPBF 316H and aged versions of this alloy further validates the correlations in literature and, through the delineation of BD and TD, provides an assessment of the effect of texture on these relationships. However, these empirical correlations are limited. In all studies cited, the correlation is presented considering an estimated plastic strain of about 8% for the volume deformed by the Vickers indenter. Thus, in materials with significant work hardening, such as nickel alloys, the stress estimated from these correlations will overestimate the 0.2% offset YS and additional work to determine the stress exponent and extrapolate from 8% to 0.2% would be needed [24]. In the case of these correlations, the value of about 3× was derived from irradiated materials [23],

small-grain and irradiated materials [21], pure metals such as copper and aluminum [22], and, in this work, materials with initially high dislocation densities and precipitates. The mixture of work-hardening materials and non-work-hardening steels suggests this correlation is universal across metals and alloys and can be used to equate the nanohardness to the Vickers hardness.

3.2 A RELATIONSHIP BETWEEN VICKERS HARDNESS AND NANOHARDNESS

The previous section validates a long-standing relationship between the YS and Vickers hardness for LPBF 316H and aged variants of LPBF 316H. The next reduction in length scale is obtained by using instrumented indentation testing or "nanoindentation." Although both hardness techniques use a pyramidal tip to indent the surface of a material, the larger cross-sectional area and force applied during loading (~1.96 N) for Vickers hardness makes minor surface variations from polishing, oxidation, or etching negligible. However, for nanoindentation where the tip is smaller and the applied force is on the order of millinewtons, minor variations in surface condition are expected to cause significant scatter in the resulting hardness profiles.

To examine the effect of surface roughness, a commercial heat of wrought 316H (heat 311373 from Sandmeyer Steel Company) was polished using standard metallographic procedures decreasing in particle size to five surface finishes: 3 μm roughness from a diamond solution, 1 μm roughness from a diamond solution, 0.5 μm roughness from a diamond solution, 0.02 μm roughness from a colloidal silica solution, and an electrolytic etch with oxalic acid. The roughest and finest surfaces are compared in Figure 5 as hardness plotted against the indentation depth, a Nix–Gao plot based on Eq. (4), and the measured elastic modulus. Following the Nix–Gao analysis method in Section 2.2, hardness from each level of surface finish was extrapolated to a bulk-like hardness compared in Table 1 along with the elastic modulus. As the plots and table show, the bulk-equivalent hardness in each case is identical within the uncertainty bounds. Therefore, bulk-equivalent properties in this circumstance did not depend significantly on the level of surface finish within the study set. However, this result does not mean all measurements will be immune from the effects of the surface finish, as demonstrated with the elastic modulus measurements, and especially those with distinct properties between the surface and the substrate (i.e., ion-bombarded surfaces). The success of this polishing study helps derive the relationship that will be used for the ion-irradiated specimens later in this report.

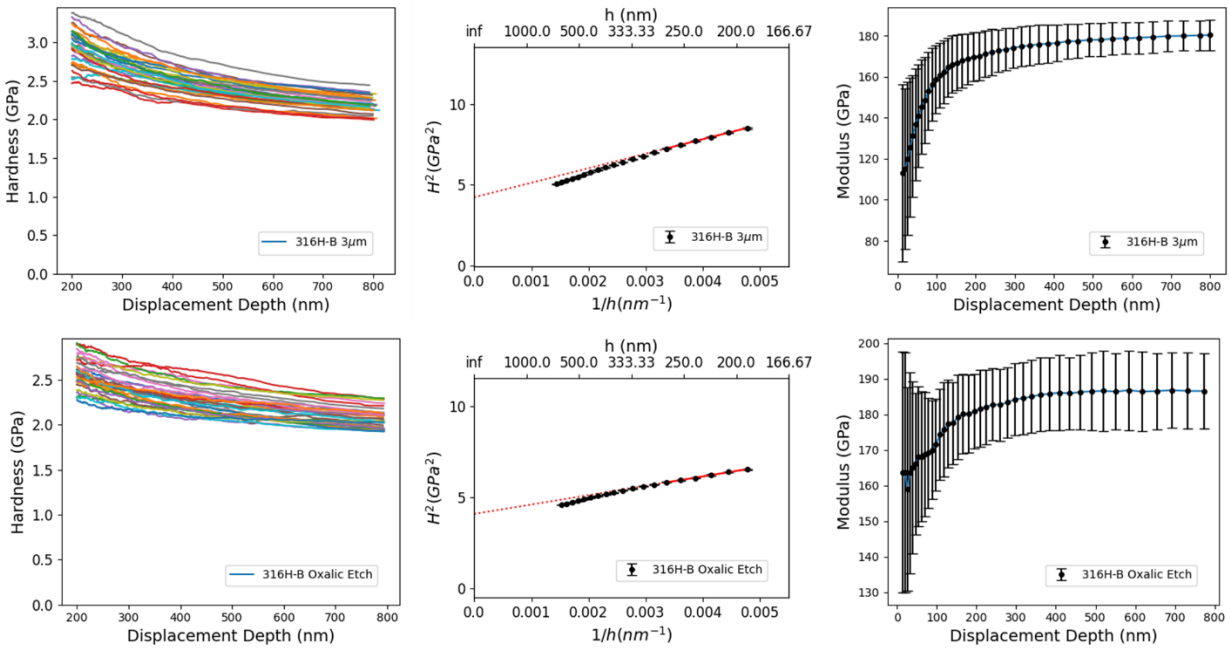

Figure 5. Surface roughness comparison. (left) Nanohardness, (center) Nix–Gao plots, and (right) measured elastic modulus for 316H polished (top row) to a 3 μm finish or (bottom row) with an electrolytic oxalic acid etch.

Table 1. Comparison of measured bulk equivalent hardness and modulus for wrought 316H with progressively smaller surface finishes. Values calculated using data from 200 to 300 nm from the surface.

Final surface finish	Hardness, H_0 (GPa)	Modulus (GPa)
3 μm diamond	2.05 ± 0.17	163.2 ± 15.0
1 μm diamond	1.98 ± 0.26	156.6 ± 19.0
0.5 μm diamond	1.95 ± 0.15	169.6 ± 13.7
Electron backscatter diffraction (0.02 μm colloidal silica)	2.02 ± 0.25	185.5 ± 8.9
Electrolytic oxalic acid etch	2.02 ± 0.23	178.5 ± 14.1

With the success of the previous polishing study, the same nanoindentation parameters and processes were applied to aged 316H specimens where Vickers hardness data existed. Representative Nix–Gao plots for 650°C, 750°C, and 850°C aged for 6 h are shown in Figure 6 along with the as-printed LPBF 316H. Following the determination of the bulk equivalent hardness, H_0, for each condition, the hardness was converted from gigapascals to the units of kilogram-force per square millimeter for Vickers hardness. The literature has shown that a pileup correction is needed to convert nanohardness to Vickers hardness [12], and the same methodology was applied to this work. The pileup-corrected hardness values from nanoindentation are plotted against the measured Vickers hardness in Figure 7 and shown in

Table 2. Within the error bars, the pileup-corrected bulk hardness from nanoindentation and the Vickers hardness are generally in agreement. The correlation may require further development because the nanoindentation hardness is consistently higher than the measured Vickers hardness. Nevertheless, this relationship serves as the first approximation that, with the correlation from the previous section, allows conversion of nanoindentation results to YS within a reasonable uncertainty.

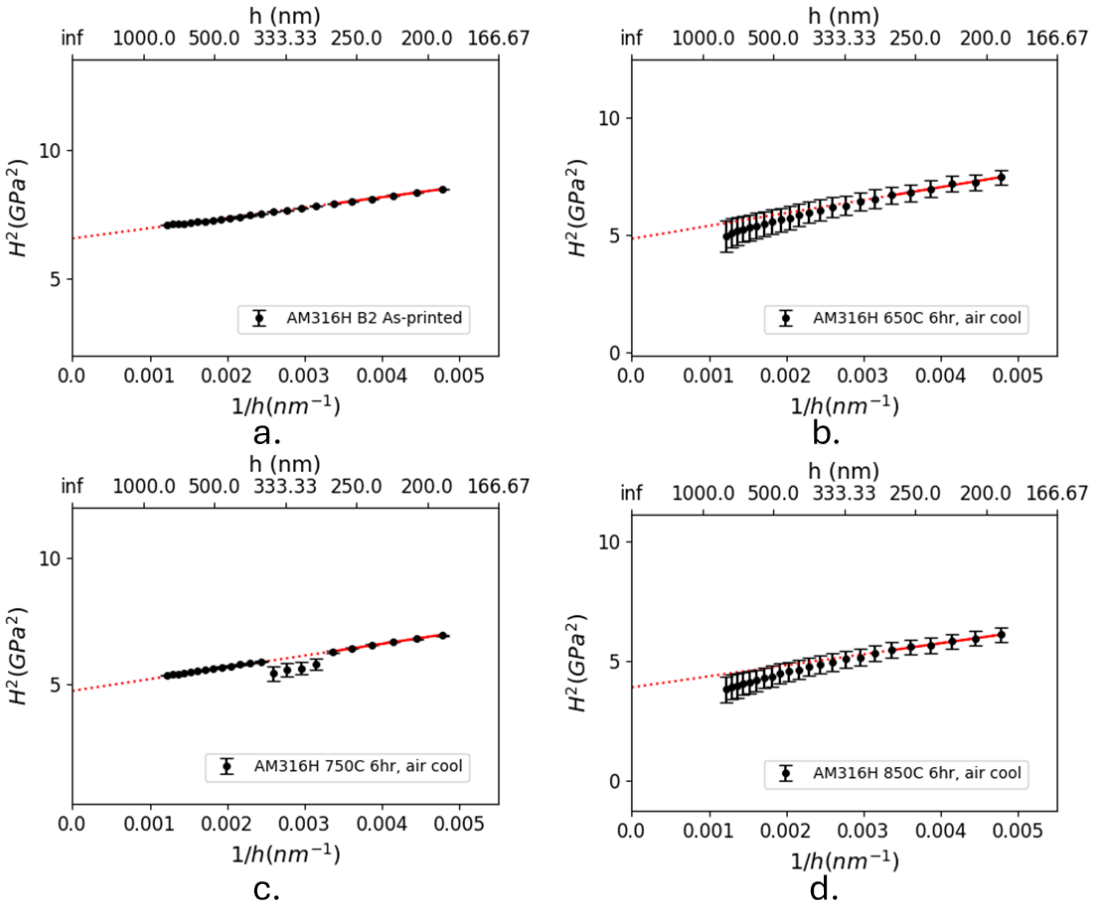

Figure 6. Nix–Gao plots. (a) As-printed LPBF 316H and LPBF 316H aged for 6 h at (b) 650°C, (c) 750°C, and (d) 850°C.

Table 2. Comparison of nanoindentation hardness, calculated Vickers hardness, and measured Vickers hardness for several conditions of LPBF 316H.

Condition	Temperature (°C)	Aging time (h)	H_0 from nanoindentation with pileup corrections (GPa)	Vickers hardness, calculated from H_0 with pileup corrections (kgf/mm^2)	Vickers hardness, measured (kgf/mm^2)
As-printed	N/A	N/A	2.2 ± 0.14	208.9 ± 13.1	215 ± 7
Aged	650	1	2.1 ± 0.13	209.0 ± 13.1	200 ± 6.9
Aged	650	2	2.1 ± 0.14	211.9 ± 13.9	198 ± 4.6
Aged	650	6	1.9 ± 0.33	199.3 ± 35.1	200 ± 6.5
Aged	750	0.5	2.0 ± 0.09	198.1 ± 8.7	187 ± 6.4
Aged	750	6	1.9 ± 0.23	183.2 ± 22.8	184 ± 5.1
Aged	850	0.25	1.9 ± 0.15	193.3 ± 15.5	179 ± 5.2
Aged	850	2	2.0 ± 0.21	199.9 ± 21.6	177 ± 6.0
Aged	850	6	1.7 ± 0.25	176.1 ± 25.7	175 ± 5.2

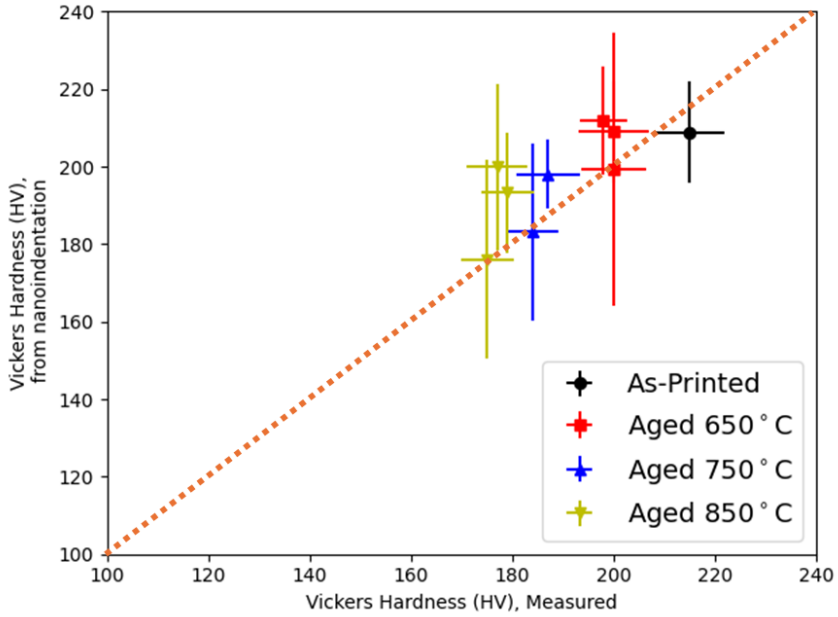

Figure 7. The correlation between measured Vickers hardness and pileup-corrected Vickers hardness from nanoindentation. The dotted line is the ideal case of equivalence between the two datasets.

4. EXTRAPOLATION TO ION-IRRADIATED MATERIALS

One of the challenges to accelerate materials qualification efforts using ion irradiation data is the ability to extract relevant mechanical property information from the thin volume that is the ion-bombarded surface. Several studies have pursued qualitative and quantitative measures with varying levels of success: one study reported a strong agreement between ion irradiation and fast reactor irradiated steel [13]. For this initial investigation, several variations of LPBF 316L and LPBF 316H were ion-irradiated at the Michigan Ion Beam Laboratory (MIBL) using 9 MeV Ni^{3+} ions at temperatures near 300°C or 600°C. Details of the ion irradiations were reported previously [8] and are not repeated here. For this report, the focus is narrowed to the LPBF 316H specimens where the materials were identical before irradiation with either neutrons in HFIR or ions at MIBL. As with previous sections, nanoindentation was conducted

using the continuous stiffness method with a frequency of 110 Hz and a variable amplitude of oscillation in proportion to 10% of the load. Because the microstructure depth examined is about 5× the indentation depth [25], the fitting for the Nix–Gao analysis was limited to 200–300 nm from the surface, corresponding to the depth at which the damage (dpa) was calculated.

Representative Nix–Gao plots for the solution-annealed (SA, 1 h at 1100°C) and stress-relieved (SR, 24 h at 650°C) LPBF 316H are included in Figure 8 for 300°C and Figure 9 for 600°C, showing the averaged values obtained from the thermal-only region, 2 dpa region, and 10 dpa region of the ion irradiated steels. The *y*-intercepts in these plots represent the square of the bulk hardness, and by comparison, they provide qualitative insight into the changes in hardness. For a temperature of either 300°C or 600°C and a time at temperature of about 8 h, the SR LPBF 316H had an higher hardness than the SA LPBF 316H, as expected based on the cellular structure still present in the SR condition, as shown for an aging time of 650°C for 1 h [18]. At 300°C, the Nix–Gao plots depict two distinct regions corresponding to the ion-irradiated volume (up to 350 nm of indentation depth) and the underlying substrate. By fitting Eq. (3) to only the ion-bombarded volume, SA and SR LPBF 316H both experienced increases in hardness at 2 dpa and nearly identical hardness at 10 dpa, suggesting a saturation in properties, as expected for this irradiation temperature [26, 27], likely from the formation of dislocation loops [19, 28]. At the higher temperature of 600°C, the LPBF is in the regime for cavity nucleation and swelling [8, 29] with fewer dislocation loops compared to the lower temperature [19]. Thus, the trend of hardness increasing with damage (dpa) is expected as the cavities continue to nucleate and grow.

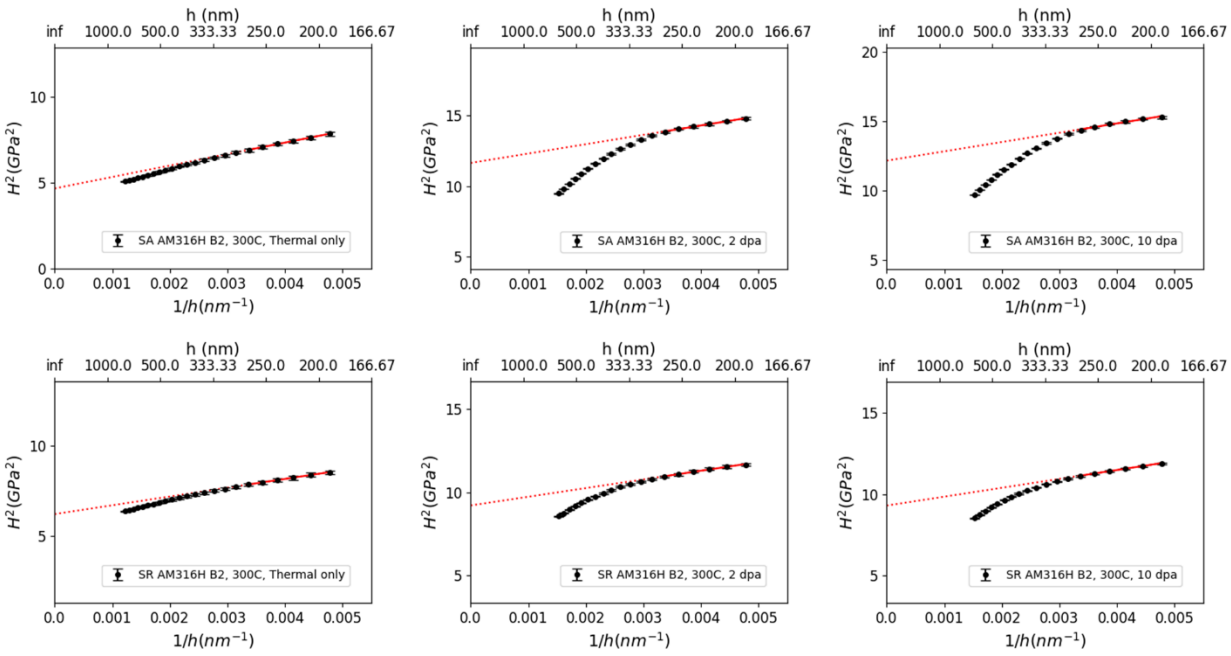

Figure 8. Nix–Gao analysis plots from ion irradiation at 300°C. Shown is the evolution of hardness for (top row) SA LPBF 316H Build 2 and (bottom row) SR LPBF 316H Build 2 for (left) the thermal-only region, (center) 2 dpa region, and (right) 10 dpa region.

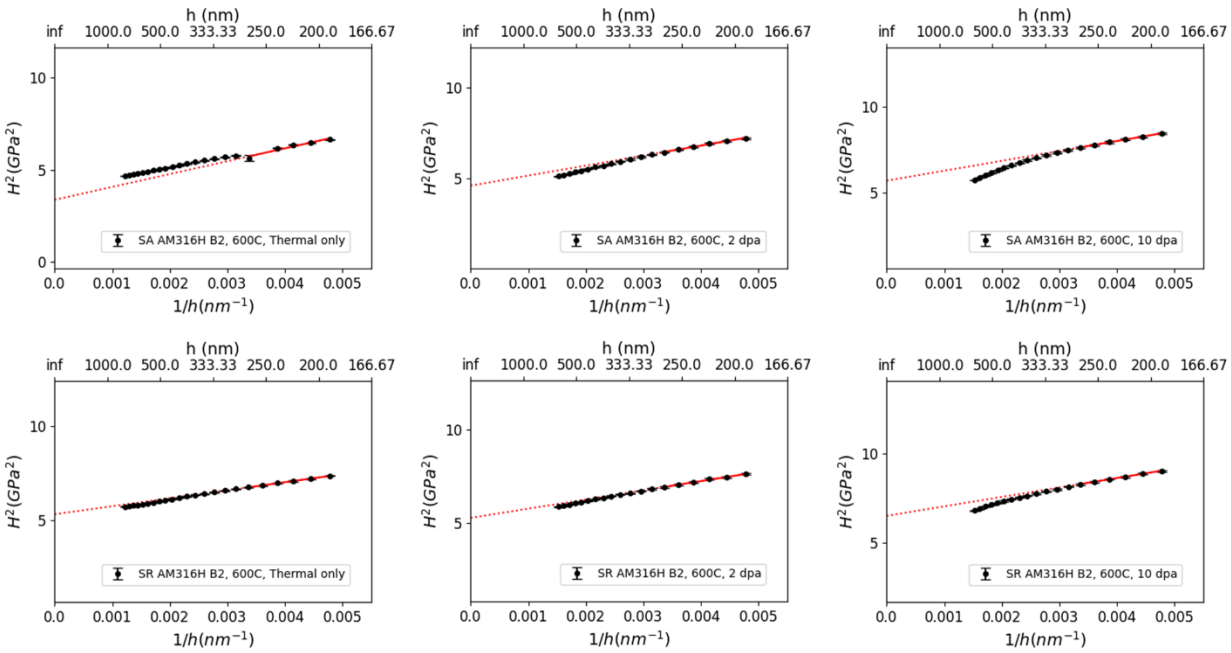

Figure 9. Nix–Gao analysis plots from ion irradiation at 600°C. Shown is the evolution of hardness for (top row) SA LPBF 316H Build 2 and (bottom row) SR LPBF 316H Build 2 for (left) the thermal only region, (center) 2 dpa region, and (right) 10 dpa region.

Bulk equivalent hardness for both the LPBF 316H Build 1 (B1) and Build 2 (B2) conditions and wrought 316H, using the correlations validated Sections 2 and 3 of this report, is used to convert H_0 to Vickers hardness with a pileup correction and then to a calculated YS. The results are shown in Table 3 with preliminary estimations of the uncertainty. Future efforts will examine the sources and propagations of uncertainty, but for now, a conservative approach has been taken. As a reminder, these results were acquired at room temperature. The same calculated YS data are plotted in Figure 10 as a function of irradiation temperature along with the HFIR-irradiated LPBF 316H in the same conditions from the literature [30]. However, this plot should be interpreted with some caution. The increased damage rate for the ion irradiations (~500× to 1000× that of the neutron damage rate) suggests that, for direct comparison, the ion irradiation "temperature" should be shifted to be lower by about 60°C–70°C [31, 32] or more [33, 34]. However, with only two temperatures for each of the neutron and ion irradiation datasets, the temperature shift needed to compensate for this damage rate change is speculative at best.

Direct observation of the calculated ion-irradiation YS and measured neutron-irradiation yield stress at 2 dpa shows that both datasets exhibit the same trend with irradiation temperature and overlap within an acceptable band of stress values. With the 300°C ion irradiations at a lower temperature than the approximately 400°C neutron irradiations, the relatively higher YS was expected. At the higher temperatures, the ion and neutron samples are in strong agreement and nearly identical within error. Additionally, the 10 dpa values for ion irradiation are plotted to serve as a prediction of properties. Postirradiation examination of HFIR-irradiated LPBF 316H up to 10 dpa is planned for future years, and thus this postirradiation examination could serve as a validation dataset for the predictions from ion irradiation.

Table 3. Measured bulk-equivalent hardness values with the conversion to Vickers hardness and YS for 9 MeV ion-irradiated 316H steels. The values for 0 dpa and 0°C irradiation temperature indicate the thermal-only region on the ion-bombarded sample.

Alloy	Processing	Heat treatment	Damage (dpa)	Irradiation temperature (°C)	H_0 (GPa)	Vickers hardness with pileup corrections (kgf/mm^2)	Calculated YS (MPa)
316H	LPBF B1	SA	0	0	1.90 ± 0.27	171.0 ± 24.7	215 ± 73
316H	LPBF B1	SR	0	0	2.56 ± 0.26	240.8 ± 24.7	422 ± 73
316H	LPBF B1	SR	0	0	2.53 ± 0.23	216.6 ± 20.1	350 ± 60
316H	LPBF B2	SA	0	0	1.83 ± 0.62	173.1 ± 58.5	221 ± 173
316H	LPBF B2	SR	0	0	2.31 ± 0.16	197.5 ± 14.1	294 ± 42
316H	LPBF B2	SA	0	0	2.16 ± 0.26	189.2 ± 22.5	269 ± 67
316H	LPBF B2	SR	0	0	2.49 ± 0.23	211.7 ± 19.6	336 ± 58
316H	Wrought	SA	0	0	2.21 ± 0.24	187.3 ± 20.7	264 ± 61
316H	LPBF B1	SA	2	600	2.04 ± 0.20	192.0 ± 19.0	278 ± 56
316H	LPBF B1	SR	2	600	2.58 ± 0.33	224.1 ± 28.3	373 ± 84
316H	LPBF B2	SA	2	300	3.41 ± 0.32	302.0 ± 28.4	603 ± 84
316H	LPBF B2	SR	2	300	3.03 ± 0.31	267.1 ± 27.4	500 ± 81
316H	LPBF B2	SA	2	600	2.14 ± 0.28	198.2 ± 25.9	296 ± 77
316H	LPBF B2	SR	2	600	2.30 ± 0.28	208.4 ± 25.4	326 ± 75
316H	Wrought	SA	2	600	2.36 ± 0.30	200.0 ± 25.1	301 ± 74
316H	LPBF B1	SR	10	300	3.14 ± 0.29	268.7 ± 24.7	505 ± 73
316H	LPBF B1	SA	10	600	2.32 ± 0.25	210.2 ± 22.7	331 ± 67
316H	LPBF B1	SR	10	600	2.37 ± 0.29	211.2 ± 26.1	334 ± 77
316H	LPBF B2	SA	10	300	3.49 ± 0.48	308.0 ± 42.1	621 ± 125
316H	LPBF B2	SR	10	300	3.05 ± 0.28	269.0 ± 24.5	506 ± 73
316H	LPBF B2	SA	10	600	2.38 ± 0.24	218.0 ± 2.22	354 ± 66
316H	LPBF B2	SR	10	600	2.55 ± 0.20	222.0 ± 17.6	366 ± 52
316H	Wrought	SA	10	600	2.51 ± 0.25	212.6 ± 21.5	339 ± 63

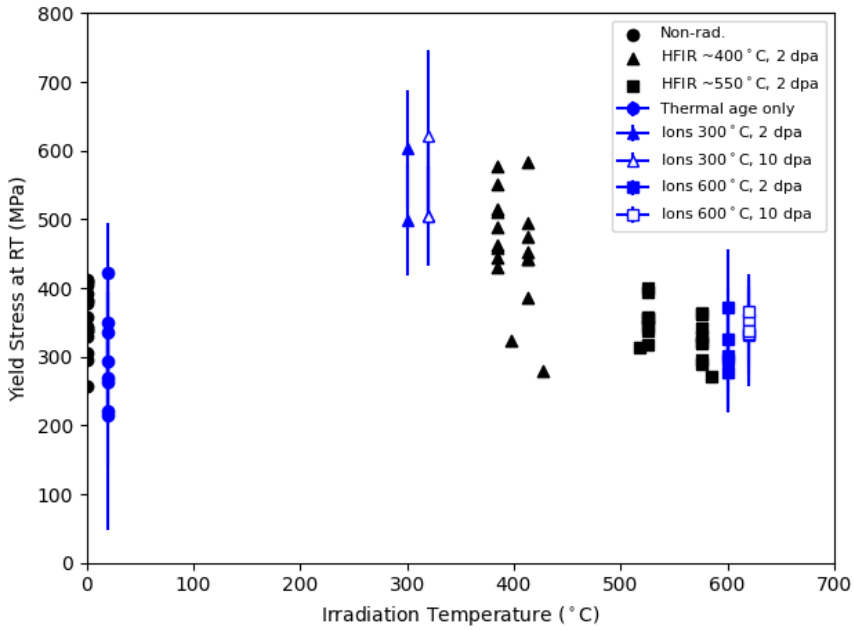

Figure 10. Comparison of the yield stress at room temperature for LPBF 316H from neutron irradiation (HFIR) and 9 MeV Ni^{3+} ion irradiation. The ion irradiation data for room temperature and at 10 dpa have been displaced for visibility.

The trends illustrated in Figure 10 do not imply the equivalence in microstructures between the ion-irradiated and the HFIR-irradiated LPBF 316 stainless steels. In fact, previous work noted several differences across the dislocation, cavity, and precipitate microstructures [8]. A possible explanation for the similarity in trends stems from the superposition of strong and weak obstacles in the microstructure. In general, the contribution of microstructure features to the YS ($\Delta\sigma$) through an Orowan mechanism is described by Eq. (5), where α is the strength of the obstacle from 0 to 1, M is the Taylor factor and represents an upper limit at 3.06 [35], μ is the shear modulus, b is the Burgers vector, d is the size of the obstacle, and N is the density of the obstacle.

$$\Delta\sigma = \alpha M \mu b \sqrt{Nd}. \#(5)$$

The superposition of weak and strong obstacles is generally described by separating the two groups at a cutoff in the value of α, nominally 0.25, followed by computing a root sum square for each class, and then performing a linear superposition to combine the strengths [10]. Additional mechanisms such as the Hall–Petch relationship and Peierls stress need to be included with the microstructure features. When a dislocation segment bows out under an applied stress between two strong obstacles, it likely will cut through any weak obstacles in its path before overcoming the strong obstacles [36]. Thus, the strong obstacles tend to dominate the response under stress. Further discussion of the links between microstructure and YS are in the following section.

5. DIRECTLY LINKING MICROSTRUCTURES TO YIELD STRESS

As highlighted in the introduction to this report, a direct pathway from the microstructure to the YS from neutron-irradiated, ion irradiated, or as-manufactured steels would be ideal. A direct expression from the microstructures to the YS is complex given the variety of microstructural features. As mentioned in the previous section, the variation in the contributions to YS stem primarily from the strength (α), size (d), and density of obstacles (N). Tan and Busby [11] summarized how the strength factor can be estimated

from aligned thin-plate shaped features like dislocation loops (Eq. (6)), precipitates with varying coherency and shape (Eqs. (7), (8), and (9)) and cavities (Eq. (10)). When obstacles have similar strengths, they are combined using a root mean sum approach (Eq. (11)) and using a linear approach when the strengths are dissimilar (Eq. (12)). The specific terms in each equation are detailed elsewhere [11]. That these equations do not refer to the temperature and neglect any thermal contributions to the strength of an obstacle or the ability for a dislocation to climb over an obstacle as opposed to shearing through the obstacle.

$$\alpha_{pp} = \frac{0.271A}{(1-\nu)^2\sqrt{ND}(16-\pi tA)} \ln\left(\frac{0.637D}{r_0}\right) \#(6)$$

$$\alpha_{CP} = \frac{0.816\gamma_{cp}d}{\mu b^2(1-0.816d\sqrt{Nd})} + 1.7\left(\frac{d}{b}\right)^{1.5}\varepsilon^{1.5} + 0.0054\left(\frac{d}{b}\right)^{0.275}\left(\frac{\Delta\mu}{\mu}\right)^{1.5} \#(7)$$

$$\alpha_{RP} = \frac{0.0957\sqrt{l/\delta}}{(1-\nu)^2(1-\delta\sqrt{Nl})} \ln\left(\frac{1.414\delta}{r_0}\right) \#(8)$$

$$\alpha_{SP} = \frac{0.135}{(1-\nu)^2(1-d\sqrt{Nd})} \ln\left(\frac{0.816d}{r_0}\right) \#(9)$$

$$a_{pp} = \frac{0.217A}{(1-\nu)^2\sqrt{ND}(16-\pi tA)} \ln\left(\frac{0.637D}{r_0}\right) \#(10)$$

$$\Delta\sigma_y = \sqrt{\sum_i^n \left(\Delta\sigma_{y,i}\right)^2} \#(11)$$

$$\Delta\sigma_y = \sum_i^n \Delta\sigma_{y,i} \#(12)$$

These equations, along with Eq. (5) provide several possible ways to combine the microstructural features into an estimated YS, as illustrated schematically in Figure 11. The common approach is to use average values for the microstructural feature of interest. In many cases, the strength parameter, α, is used as a fitting value to force an agreement between the microstructure and YS. A recent approach used a linear least squares approach to compare α values calculated from the microstructure with those calculated using Eqs. (6)–(10) [37], showing that an agreement could be reached if the strain field around a dislocation core is included instead of only the dislocation core itself. The next common approach is to apply a weight to the contributions by their density or use a median value for the size. This approach considers more aspects of the size distribution than the previous approach, but likely still results in inaccuracies. The next approach is the integral approach where the size distribution is divided into equal bins and the contributions to YS are calculated based on the strength, size, and density of the individual bin. In theory, this approach better captures the contributions of smaller and larger precipitates than the average or weighted average approaches. However, this approach still results in one value for the calculated YS. The final presented approach is dubbed a Monte Carlo approach. In this approach, the size distribution is still divided into individual bins. To calculate YS, a random bin is selected for each microstructure feature to represent the statical nature of dislocation interactions. YS is calculated from randomized contributions until a distribution of YS is obtained. The Monte Carlo approach was used previously to link the

microstructure of 14YWT to its yield properties [38] with limited success, noting the limitations of characterization techniques to accurately determine the size distribution of a microstructure feature. In these approaches, microstructure characterization is necessary for most features. Because these data are not yet available from the microstructure or modeling sides of the irradiation challenge problem, determining the link using these approaches is left for future work.

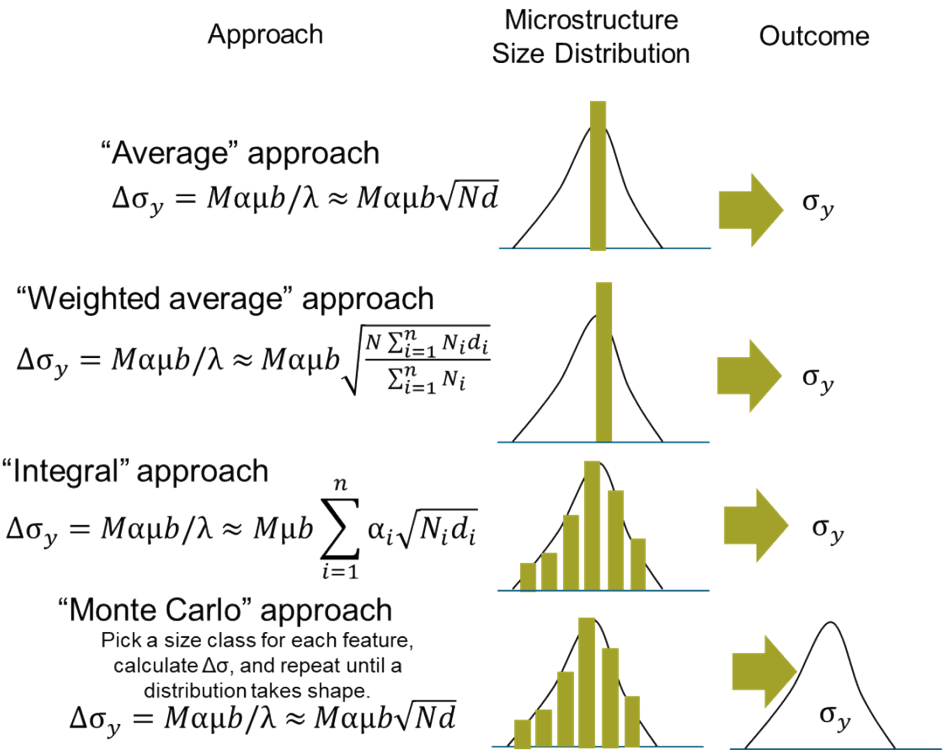

Figure 11. Approaches to combine microstructural features into an estimated YS.

6. CONCLUSIONS

The overall goal in FY 2025 was to exercise the irradiation challenge program by generating initial predictions of neutron irradiated hardness or YS at 10 dpa for one LPBF 316 steel ion-irradiated at 600°C. As demonstrated in Section 4, the simple mathematical correlations developed in Section 3 from aged LPBF 316H stainless steels allowed extrapolation of the nanoindentation hardness of ion-irradiated steels to form the same trend and order of magnitude as the HFIR-irradiated steels. However, although these correlations provide some predictive measures, the microstructural origins are not yet known. Further characterization of irradiated materials in the AMMT program will serve as foundational datasets to develop further predictive mechanical models. Additionally, tensile testing of the HFIR-irradiated LPBF 316H at 10 dpa will confirm or refute the predictions made through ion irradiations. This work demonstrates that the LAIN approach can generate mechanical property information using ion irradiations, and this process is faster than using neutron irradiations.

7. REFERENCES

[1] *BPVC.III.5 - BPVC Section III-Rules for Construction of Nuclear Facility Components-Division 5-High Temperature Reactors*. ASME, 2025.

[2] R. N. Wright, "Updated Draft ASME Boiler and Pressure Vessel Code Case for Use of Alloy 617 for Construction of Nuclear Components for Section III Division 5," Idaho Falls, ID (United States), 2018. [Online]. Available: http://www.osti.gov/servlets/purl/1471711/

[3] R. H. Howard, D. Chandler, A. G. Le Coq, S. A. Taller, K. D. Linton, and M. N. Cinbiz, "The state of the art for neutron irradiation experiments from the perspective of the High Flux Isotope Reactor (HFIR)," *Nuclear Engineering and Design,* vol. 444, 2025, doi: 10.1016/j.nucengdes.2025.114401.

[4] D. Collins, M. Gussev, S. Taller, T. S. Byun, and C. Massey, "Assessing the viability of a new subsize tensile specimen geometry for evaluation of structural nuclear and additively manufactured materials," *Journal of Nuclear Materials,* vol. 612, 2025, doi: 10.1016/j.jnucmat.2025.155831.

[5] E. O. o. t. President, "Deploying Advanced Nuclear Reactor Technologies for National Security," *Federal Register,* vol. 90, no. 102, p. 22581, May 23 2025.

[6] S. Taller, Y. Chen, R. Song, W.-Y. Chen, and A. Jokisaari, "An approach to combine neutron and ion irradiation data to accelerate material qualification for nuclear reactors," *Journal of Nuclear Materials,* vol. 603, 2025, doi: 10.1016/j.jnucmat.2024.155385.

[7] A. Jokisaari, W. Chen, Y. Chen, R. Song, and S. Taller, "Promoting the Regulatory Acceptance of Combined Ion and Neutron Irradiation for Material Degradation in Nuclear Reactors," OSTI, 2023.

[8] S. Taller *et al.*, "Report on the Integration of Experimental and Modeling Data for Initial Equivalence Study of Microstructural Evolution in Irradiated LPBF 316SS," Oak Ridge National Laboratory, Oak Ridge, TN, ORNL/TM-2024/3580, 2024.

[9] F. Mudry, "A local approach to cleavage fracture," *Nuclear Engineering and Design,* vol. 105, no. 1, pp. 65-76, 1987, doi: 10.1016/0029-5493(87)90230-5.

[10] P. Zhu, Y. Zhao, Y.-R. Lin, J. Henry, and S. J. Zinkle, "Defect-specific strength factors and superposition model for predicting strengthening of ion irradiated Fe18Cr alloy," *Journal of Nuclear Materials,* vol. 588, 2024, doi: 10.1016/j.jnucmat.2023.154823.

[11] L. Tan and J. T. Busby, "Formulating the strength factor α for improved predictability of radiation hardening," *Journal of Nuclear Materials,* vol. 465, pp. 724-730, 2015, doi: 10.1016/j.jnucmat.2015.07.009.

[12] P. Zhu, Y. Zhao, S. Agarwal, J. Henry, and S. J. Zinkle, "Toward accurate evaluation of bulk hardness from nanoindentation testing at low indent depths," *Materials & Design,* vol. 213, 2022, doi: 10.1016/j.matdes.2021.110317.

[13] P. Zhu, Y.-R. Lin, S. Agarwal, V. Pauly, S. Taller, and S. J. Zinkle, "Comparison of hardening and microstructures of ferritic/martensitic steels irradiated with fast neutrons and dual ions," *Journal of Nuclear Materials,* vol. 599, 2024, doi: 10.1016/j.jnucmat.2024.155211.

[14] M. Li, D. Andersson, R. Dehoff, A. Jokisaari, I. van Rooyen, and D. Cairns-Gallimore, "Department of Energy Office of Nuclear Energy Advanced Materials and Manufacturing Technologies (AMMT) 2022 Roadmap," Argonne National Laboratory, 2022.

[15] G. M. Pharr, E. G. Herbert, and Y. Gao, "The Indentation Size Effect: A Critical Examination of Experimental Observations and Mechanistic Interpretations," *Annual Review of Materials Research,* vol. 40, no. 1, pp. 271-292, 2010, doi: 10.1146/annurev-matsci-070909-104456.

[16] J. Hay, P. Agee, and E. Herbert, "Continuous Stiffness Measurement during Instrumented Indentation Testing," *Experimental Techniques,* vol. 34, no. 3, pp. 86-94, 2010, doi: 10.1111/j.1747-1567.2010.00618.x.

[17] W. D. Nix and H. Gao, "Indentation size effects in crystalline materials: A law for strain gradient plasticity," *Journal of the Mechanics and Physics of Solids,* vol. 46, no. 3, pp. 411-425, 1998, doi: 10.1016/s0022-5096(97)00086-0.

[18] G. Kumari *et al.*, "Post-build stress-relief optimization for laser powder bed fusion 316H stainless steel," *Materialia,* vol. 43, 2025, doi: 10.1016/j.mtla.2025.102520.

[19] W.-Y. Chen *et al.*, "Characterization of in-situ and ex-situ ion-irradiated additively manufactured 316L and 316H stainless steels," *Journal of Nuclear Materials,* vol. 616, 2025, doi: 10.1016/j.jnucmat.2025.156044.
[20] R. Kannan, T. Feldhausen, and P. Nandwana, "Microstructure manipulation via machining and heat treatments in hybrid manufacturing of 316L stainless steel," *Manufacturing Letters,* vol. 40, pp. 65-69, 2024, doi: 10.1016/j.mfglet.2024.02.004.
[21] D. L. Krumwiede, T. Yamamoto, T. A. Saleh, S. A. Maloy, G. R. Odette, and P. Hosemann, "Direct comparison of nanoindentation and tensile test results on reactor-irradiated materials," *Journal of Nuclear Materials,* vol. 504, pp. 135-143, 2018, doi: 10.1016/j.jnucmat.2018.03.021.
[22] D. Tabor, "The physical meaning of indentation and scratch hardness," *British Journal of Applied Physics,* vol. 7, no. 5, pp. 159-166, 1956, doi: 10.1088/0508-3443/7/5/301.
[23] J. T. Busby, M. C. Hash, and G. S. Was, "The relationship between hardness and yield stress in irradiated austenitic and ferritic steels," *Journal of Nuclear Materials,* vol. 336, no. 2-3, pp. 267-278, 2005, doi: 10.1016/j.jnucmat.2004.09.024.
[24] J. R. Cahoon, W. H. Broughton, and A. R. Kutzak, "The determination of yield strength from hardness measurements," *Metallurgical Transactions,* vol. 2, no. 7, pp. 1979-1983, 1971, doi: 10.1007/bf02913433.
[25] L. E. Samuels and T. O. Mulhearn, "An experimental investigation of the deformed zone associated with indentation hardness impressions," *Journal of the Mechanics and Physics of Solids,* vol. 5, no. 2, pp. 125-134, 1957, doi: 10.1016/0022-5096(57)90056-x.
[26] D. R. Harries, "Neutron irradiation-induced embrittlement in type 316 and other austenitic steels and alloys," *Journal of Nuclear Materials,* vol. 82, no. 1, pp. 2-21, 1979, doi: 10.1016/0022-3115(79)90034-5.
[27] J. Garnier *et al.*, "Deformation Under Irradiation of 304L and 316 Austenitic Steels," in *13th International Conference on Environmental Degradation of Materials in Nuclear Power Systems*, Whistler, British Columbia, 2007 2007, vol. 1, pp. 241-253.
[28] S. J. Zinkle, "Radiation-Induced Effects on Microstructure," in *Comprehensive Nuclear Materials*, vol. 1: Elsevier, 2020, pp. 91-129.
[29] A. Bhattacharya and S. J. Zinkle, "Cavity Swelling in Irradiated Materials," in *Comprehensive Nuclear Materials*, vol. 1: Elsevier, 2020, pp. 406-455.
[30] C. Massey *et al.*, "Low-Dose Neutron Irradiation Effects on Mechanical Properties of Additively Manufactured SS-316," ORNL/SPR-2025/3773, March 2025 2025.
[31] S. Taller, Z. Jiao, K. Field, and G. S. Was, "Emulation of fast reactor irradiated T91 using dual ion beam irradiation," *Journal of Nuclear Materials,* vol. 527, pp. 151831-151831, 2019, doi: 10.1016/j.jnucmat.2019.151831.
[32] S. Taller, G. VanCoevering, B. D. Wirth, and G. S. Was, "Predicting structural material degradation in advanced nuclear reactors with ion irradiation," *Scientific Reports,* vol. 11, no. 1, pp. 2949-2949, 2021, doi: 10.1038/s41598-021-82512-w.
[33] L. K. Mansur, "Correlation of neutron and heavy-ion damage. II. The predicted temperature shift if swelling with changes in radiation dose rate," *Journal of Nuclear Materials,* vol. 78, no. 1, pp. 156-160, 1978, doi: 10.1016/0022-3115(78)90514-7.
[34] L. K. Mansur, "Theory of transitions in dose dependence of radiation effects in structural alloys," *Journal of Nuclear Materials,* vol. 206, no. 2-3, pp. 306-323, 1993, doi: 10.1016/0022-3115(93)90130-Q.
[35] R. E. Stoller and S. J. Zinkle, "On the relationship between uniaxial yield strength and resolved shear stress in polycrystalline materials," *Journal of Nuclear Materials,* vol. 283-287, no. PART I, pp. 349-352, 2000, doi: 10.1016/S0022-3115(00)00378-0.
[36] U. F. Kocks, "A Statistical Theory of Alloy Hardening," in *Physics of Strength and Plasticity*, A. S. Argon Ed. Cambridge, Massachusetts: MIT Press, 1969.

[37] S. Taller and T. Austin, "Using post-processing heat treatments to elucidate precipitate strengthening of additively manufactured superalloy 718," *Additive Manufacturing,* vol. 60, 2022, doi: 10.1016/j.addma.2022.103280.
[38] C. P. Massey *et al.*, "Insights from microstructure and mechanical property comparisons of three pilgered ferritic ODS tubes," *Materials & Design,* vol. 213, 2022, doi: 10.1016/j.matdes.2021.110333.